

1 **In situ ultrathin silica layer formation on polyamide thin-film composite membrane**
2 **surface for enhanced forward osmosis performances**

3

4 Nawshad Akther^a, Yuqing Lin^b, Shengyao Wang^b, Sherub Phuntsho^a, Qiang Fu^a, Noredine
5 Ghaffour^c, Hideto Matsuyama^b, and Ho Kyong Shon^{a*}

6

7 ^a School of Civil and Environmental Engineering, University of Technology Sydney (UTS),
8 NSW 2007, Australia

9 ^b Research Center for Membrane and Film Technology, Department of Chemical Science and
10 Engineering, Kobe University, 1-1 Rokkodaicho, Nada-ku, Kobe 657-8501, Japan

11 ^c King Abdullah University of Science and Technology (KAUST), Water Desalination and
12 Reuse Center (WDRC), Biological & Environmental Science & Engineering Division (BESE),
13 Thuwal, 23955-6900, Saudi Arabia

14

15

16 * Corresponding author: Prof. Hokyong Shon Email: hokyong.shon-1@uts.edu.au; Tel.: +61 2
17 9514 2629; Fax: +61 2 9514 2633.

18

19 **Keywords:** forward osmosis (FO); thin-film composite (TFC); polyamide membrane; surface
20 modification; silica nanoparticles.

21

22

23 **Abstract**

24 Polyamide (PA) based thin-film composite (TFC) membranes experience a high degree of
25 organic fouling due to their hydrophobic and rough membrane surfaces during forward osmosis
26 (FO) process. In this study, an ultrathin silica layer was grown *in situ* on the PA surface to
27 enhance the antifouling property of TFC membrane by silicification process. Surface
28 characterization confirmed the development of silica layer on the PA surface with thickness
29 and hydrophilicity intensifying with increasing silicification duration. The super hydrophilic
30 surface of silica-deposited TFC membrane (contact angle of 20°) with 3 h silicification time
31 (STFC-3h) displayed 53% higher water flux in comparison to the pristine membrane without
32 significantly compromising the membrane selectivity. The silica-modified TFC FO membrane
33 surface also exhibited excellent stability when subjected to long-term cross-flow shear stress
34 rinsing using deionized (DI) water including exposure to salty, acidic and basic solutions.
35 Moreover, the fouling tests showed that STFC-3h membrane lost only 4.2%, 9.1% and 12.1%
36 of its initial flux with bovine serum albumin (BSA), humic acid (HA) and sodium alginate
37 (SA), respectively, which are considerably lower compared to the pristine TFC FO membrane
38 where flux losses were 18.7%, 23.2% and 37.2%, respectively. The STFC-3h membrane also
39 revealed higher flux recovery ratio (FRR) of 99.6%, 96.9% and 94.4% with BSA, HA and SA,
40 respectively, after physical cleaning than the pristine membrane (91.4%, 88.7%, and 81.2%,
41 respectively). Overall, the *in situ* formation of an ultrathin hydrophilic silica layer on the PA
42 surface reported in this work shows that the TFC membrane's water flux and antifouling
43 property could be improved without diminishing the membrane selectivity.

44

45 **1 Introduction**

46 Osmotically driven membrane processes like forward osmosis (FO) have been widely
47 studied in recent decades for wastewater treatment [1], wastewater reclamation and seawater
48 dilution [2], resource recovery [3], and food processing [4] due to their high water recovery,
49 reduced fouling tendency and low energy consumption as opposed to pressure-driven
50 membrane processes like reverse osmosis (RO). FO only operates under the osmotic pressure
51 gradient existing between high salinity draw solution (DS) and the low salinity feed solution
52 (FS) streams across the semipermeable membrane [5, 6]. As a result, FO processes are
53 considered to be more energy efficient than RO when used in applications that do not require
54 DS recovery.

55 State-of-the-art aromatic polyamide (PA) thin-film composite (TFC) membranes have
56 been considered promising candidates for various separation processes due to their high degree
57 of tunability, unparalleled permeability-rejection performance, and broader pH tolerance range
58 in comparison to cellulose-based membranes [7, 8]. The PA TFC membrane consist of a PA
59 selective layer formed on top of a mechanically robust porous substrate via interfacial
60 polymerization (IP) reaction [9]. Despite being considered the benchmark for water treatment
61 membranes, the PA TFC membranes experience the trade-off between water permeability and
62 salt selectivity. Additionally, the characteristic rough and hydrophobic surface of the PA
63 selective layer increases membrane fouling propensity, which in turn severely hinders the
64 treatment of high-fouling wastewaters. Consequently, the deteriorated membrane performance
65 escalates the overall process energy requirement, operational costs, and reduces membrane life.
66 Therefore, it is imperative to design the structural and chemical properties of FO membranes
67 to prevent or reduce foulant build-up on the membrane surface, while retaining a high
68 membrane separation performance.

69 Membrane surface properties, such as high hydrophilicity and low roughness, have
70 demonstrated to play an essential role in enhancing the membrane antifouling property by
71 limiting its affinity to interact with the organic matter, thereby, reducing physisorption of
72 foulants [10]. To diminish the fouling of PA TFC membranes, researchers have developed
73 various methods such as rendering the PA layer surface smoother, making membrane surface
74 more hydrophilic and less charged through alteration of IP process[11], plasma surface
75 treatment [12], and hydrophilic macromolecule attachment via dip-coating [13], free radical
76 [14] or graft polymerizations [15]. Nonetheless, the use of above techniques is not very useful
77 because their scope for enhancing fouling control is limited. Other strategies include the
78 introduction of nanomaterials either embedded within the PA selective layer [16, 17] or coating
79 on the PA layer surface [18]. For instance, it has been observed that when nanomaterials like
80 carbon nanotubes [19], halloysite nanotubes [20], graphene oxide [21, 22] and silver
81 nanoparticles [23] are incorporated into the PA selective layer, the antifouling properties of
82 thin-film nanocomposite (TFN) membranes can be improved. However, such modification
83 methods can influence the membrane separation performance by affecting the chemical
84 property of PA, and result in inadequate use of nanomaterial surface since most of it is
85 embedded in the polymer matrix.

86 On the contrary, coating the nanoparticles on the PA layer via grafting, covalent bonding,
87 surface mineralization or layer-by-layer (LbL) assembly methods is arguably more desirable
88 for tuning membrane performance, hydrophilicity, surface roughness and charge to improve
89 chlorine resistance, delay membrane fouling and provide biocidal properties without
90 considerably varying the intrinsic membrane structures [24]. For example, Tiraferri et al.
91 imparted biocidal properties to the TFC membrane surface by binding CNTs to the PA surface
92 using amide bonds, which inactivated up to 60% of the bacteria attached to the membrane
93 within one hour [7]. Hegab et al. covalently attached antibacterial GO sheets to the TFC

94 membrane surface using hybrid and layer-by-layer (LbL) grafting techniques [25]. Yu's group,
95 on the other hand, improved the fouling resistance and water flux recovery of the membrane
96 by applying surface mineralization technique to uniformly deposit silver chloride on membrane
97 surface via an alternate soaking process (ASP); where the mineralization degree was controlled
98 by varying the number of ASP cycles [26]. Atomic layer deposition (ALD) coating using
99 trimethylaluminum was also explored to alter the TFC membrane surface for better antifouling
100 performance [27]. Although nanomaterial coating methods have been extensively utilised to
101 boost the membrane surface properties and antifouling performance, the above techniques are
102 sophisticated because they require a large amount of chemicals, and involve several
103 complicated treatment steps/cycles with exceptionally challenging operating conditions, which
104 limits their scalability. In addition, physical surface coating methods may result in leaching or
105 detachment of nanoparticles from the membrane surface, which would reduce membrane
106 functionality and induce secondary environmental pollution (e.g. leaching of toxic silver ions)
107 [28]. Moreover, uncontrolled and thick deposition of nanoparticles on the membrane surface
108 could increase mass transfer resistance and reduce water flux. Therefore, ultrathin coating
109 layers on the membrane surface with good chemical and mechanical stability are preferable to
110 reduce the water transport resistance, meanwhile preventing leaching of nanomaterials from
111 the membrane surface.

112 Silica nanoparticles have been previously used for surface modification due to their
113 hydrophilicity, widespread availability and low cost [29-34]. For instance, Huang et al. grafted
114 amine-functionalized silica nanoparticles on the nanofiltration membrane surface to augment
115 its hydrophilicity and antifouling property [35]. Zhang et al. created a superhydrophilic
116 interface structure by growing a silica layer on the polyketone substrate for treating challenging
117 oily emulsions [33]. The silica-modified membranes demonstrated exceptional antifouling
118 property against a variety of oily emulsions comprising of several pollutants like natural

119 organic materials, surfactants and proteins; and achieved a flux recovery ratio (FRR) of nearly
120 100% after a number of cycles of oily emulsion filtration.

121 In this study, we developed TFC FO membrane modified with an ultrathin silica layer on
122 the PA surface via *in situ* silicification process. The silicification process was initiated using 3-
123 aminopropyltriethoxysilane (APTES) and tetraethoxysilane (TEOS) as the silane coupling
124 agent and silica precursor, respectively. The influence of silicification time on the membrane
125 surface properties, morphology and performances was systematically examined. The silica
126 coated PA TFC membrane demonstrated a hydrophilic surface with improved antifouling
127 property. Additionally, the silicification method used in this study is comparatively facile,
128 efficient and straightforward compared to other surface modification techniques, such as LbL
129 and ALD. Unlike the polymer or hydrogel coatings on the membrane surface that heighten the
130 water transport resistance [36], the ultrathin silica layer significantly improved the membrane
131 surface hydrophilicity and water permeability without adversely affecting its selectivity.
132 Moreover, the silica layer on the TFC membrane surface demonstrated excellent stability to
133 long-term stress from cross-flow rinsing using deionized (DI) water, in addition to improved
134 fouling resistance to organic foulants. Consequently, this facile membrane surface modification
135 method can deliver valuable insights for the design and preparation of antifouling PA TFC FO
136 membranes.

137 **2 Experimental method**

138 2.1 Materials

139 Solvay supplied polysulfone pellets (PSf, Udel® P-3500). M-phenylenediamine flakes
140 (MPD, 95%), 1-methyl-2 pyrrolidone (NMP, super dehydrated), n-hexane (96%), sodium
141 chloride (NaCl, 99.5%), calcium chloride (CaCl₂, 90%), ethanol (EtOH, 99.5%), bovine serum
142 albumin (BSA, fraction V), and ammonia (25%) were procured from FUJIFILM Wako Pure

143 Chemical Corporation and used without further purification. Tetraethoxysilane (TEOS, >97%),
144 1,3,5-benzenetricarbonyl trichloride (TMC, >98%), 3-aminopropyl-triethoxysilane (APTES,
145 >98%) were bought from Tokyo Chemical Industry and employed as received. Humic acid
146 (HA) sodium salt and sodium alginate (SA, 300 cps) were supplied by Nacalai Tesque, Inc.
147 and Sigma Aldrich, respectively. Deionized water (DI, ~18 M Ω /cm, Milli-Q®, Merck) was
148 used to make DS and FS.

149 2.2 Membrane fabrication

150 The porous PSf flat sheet substrates were prepared from 12 wt% PSf dope solution
151 using the non-solvent induced phase separation (NIPS) technique, as described in our previous
152 work [16]. More details are provided in the Supporting Information (SI). TFC membranes were
153 made by developing PA selective layers on the PSf substrates through IP reaction. First, the
154 substrate was immersed in a 4 wt% MPD aqueous solution for 2.5 min, and the excess solution
155 was removed using filter paper. The amine-saturated substrate was then exposed to 0.1 wt%
156 TMC/n-hexane organic solution for 1 min to initiate the IP reaction, followed by heat treatment
157 for 5 min at 60 °C to improve the PA cross-linking degree. The prepared TFC membranes were
158 stored in DI water at 4 °C before surface modification. More information is provided in the SI.

159 2.3 Membrane surface modification

160 The APTES decoration and *in situ* silicification process on membrane surface were
161 conducted using the protocols from our previous work [33]. In short, the TFC membrane was
162 first dipped in a 2 wt% APTES solution for 16 h to endow positive charge to the PA layer. The
163 APTES decorated TFC membrane was denoted as 'APTES-TFC'. A mineral precursor solution
164 prepared by mixing 100 mL ethanol, 4 mL ammonia and 1.5 mL TEOS for 5 min was then
165 immediately contacted with the PA layer of the APTES-TFC membrane for various durations
166 (1, 3 and 5 h) to start the *in situ* silicification process. The resultant silica coated TFC

167 membranes were denoted as ‘STFC-1h’, ‘STFC-3h’ and ‘STFC-5h’ depending on the
168 silicification time. The modified membranes were gently rinsed by shaking in DI water at 50
169 rpm for 24 h to remove any loose silica particles. The resultant membranes were then kept in
170 DI water at 4 °C until use.

171 2.4 Membrane characterization

172 The PA layer and cross-sectional morphologies of all the membranes were examined
173 using field emission scanning electron microscopy (FESEM; JEOL) with a 10 mA emission
174 current and 5 kV accelerating voltage. Osmium plasma coating was applied to the samples
175 prior to SEM analysis to obtain a conductive thin film. Atomic force microscopy (AFM;
176 SPI3800 N/SPA 400, Seiko Instruments Inc.) was used in non-contact mode to measure the
177 membrane surface roughness for a scan area of 5 $\mu\text{m} \times 5 \mu\text{m}$. The surface chemical
178 compositions of the membranes were studied by X-ray photoelectron spectroscopy (XPS; JSP-
179 9010MC, JEOL) with an Al-K α radiation source (1486.6 eV), Fourier-transform infrared
180 spectroscopy with attenuated total reflectance (FTIR-ATR; Bruker), and energy-dispersive X-
181 ray spectroscopy (EDS) with an emission current and accelerating voltage of 25 mA and 12
182 kV, respectively.

183 The membrane surface hydrophilicity was determined from the water contact angles
184 measured on at least 5 random positions for each sample with a contact angle goniometer (Drop
185 Master 300, Kyowa Interface Science Co.) at room temperature. An electro-kinetic analyzer
186 (SurPASSTM 3, Anton Paar) was utilised to verify the membrane surface charge by measuring
187 the zeta potential of the membranes. The zeta potential tests were conducted at a gap height of
188 100 μm with 1 mM KCl electrolyte solution and its pH was adjusted between 3 and 10 by
189 dosing with 0.05 M NaOH and HCl solutions.

190 2.5 Membrane performance assessment

191 2.5.1 FO performance

192 A laboratory-scale FO experimental setup was utilized to establish the membrane
193 performance with an active area of 4.5 cm². The FO cell comprised of a 2.5 mm deep spacer-
194 free flow channel on either side of the membrane. A co-current flow rate of 250 mL.min⁻¹ at
195 22 °C was used for both the DS and FS during the FO tests. The membranes were examined in
196 AL-FS (active layer facing to FS) mode with DI water and 1 M NaCl as FS and DS,
197 respectively. The water flux (J_w , L.m⁻².h⁻¹) and the reverse solute flux (J_s , g.m⁻².h⁻¹) through
198 the membrane was determined from Eq. S1 and Eq. S2, respectively. The specific reverse
199 solute flux ($SRSF$, g.L⁻¹) was evaluated from J_w and J_s values to specify membrane selectivity
200 (Eq. S3). The equations utilized for assessing the membrane performance are included in the
201 SI.

202 2.5.2 Membrane intrinsic transport parameters

203 The intrinsic membrane transport parameters were obtained using cross-flow
204 laboratory-scale RO filtration system with an active membrane area of 7.06 cm². All membrane
205 samples were pre-compacted with DI water at 6 bar for 1 h at a flow rate of 9.9 mL.min⁻¹ before
206 testing to obtain a stable flux. The pressure was then reduced to 5 bar to obtain the pure water
207 flux (J) and water permeability coefficient (A , L.m⁻².h⁻¹.bar⁻¹) using the following equations:

$$J = \frac{\Delta V}{A_m \cdot \Delta t} \quad (1)$$

$$A = \frac{J}{\Delta P} \quad (2)$$

208 where ΔV (L), A_m (m²), Δt (h) and ΔP (bar) are the permeate volume, active membrane area,
209 filtration duration and applied pressure difference, respectively.

210 The DI water feed was then replaced by 10 mM NaCl solution at 5 bar to determine the
211 solute rejection (R , %) and solute permeability coefficient (B , $L.m^{-2}.h^{-1}$) using Eq. 3 and 4,
212 respectively:

$$R = \left(1 - \frac{C_p}{C_f}\right) \times 100\% \quad (3)$$

$$B = A(\Delta P - \Delta\pi) \left(\frac{1 - R}{R}\right) \quad (4)$$

213 where C_p ($g.L^{-1}$) and C_f ($g.L^{-1}$) are the solute concentration of the permeate and feed solution,
214 respectively, and $\Delta\pi$ (bar) is the osmotic pressure difference across the membrane.

215 2.5.3 Stability test

216 The stability of the silica layer was assessed using the FO setup by subjecting the
217 membrane to a cross-flow velocity of 12 cm.s^{-1} over 72 h at $20 \text{ }^\circ\text{C}$ using DI water. The
218 membranes were then tested for FO performance, and the membrane surfaces were analysed
219 for hydrophilicity by determining the water contact angles. The stability of silica layer when
220 exposed to acid (HCl, pH=3), base (NaOH, pH=10) and salt (0.5 M NaCl) solutions was
221 determined by shaking the membranes for 72 h at 70 rpm in the various solutions and measuring
222 their water contact angles.

223 2.6 Membrane fouling test

224 The membrane fouling tests done in four stages in the AL-FS mode using the FO setup.
225 Firstly, baseline tests for the membranes were run with DI water FS and NaCl DS (0.5 M to 2
226 M) to adjust the initial baseline water flux ($J_{w,0}$) to $\sim 20 \text{ L.m}^{-2}.h^{-1}$ and determine the flux decline
227 resulting from the DS dilution and J_s to FS. Secondly, accelerated fouling test was initiated at
228 similar conditions as the baseline experiment by introducing 1 g.L^{-1} of foulant (BSA, HA and
229 SA) into the FS containing 1 mM CaCl_2 . BSA, HA and SA were picked as model organic
230 foulants to represent proteins, effluent organic matter (EfOM), and polysaccharides. The flux

231 decline occurring, in this instance, resulted from the collective influence of J_s , DS dilution and
 232 membrane fouling. Both the fouling and baseline tests were conducted at a flow rate of 250
 233 mL.min⁻¹ for ~17 h to obtain a cumulative permeate volume of 75 mL. The degree of fouling
 234 was quantified from the flux decline during the fouling test ($FD_{75\text{ mL}}$) using Eq. (8) as reported
 235 earlier [37]:

$$FD_{75\text{ mL}} = \frac{\left| (J_w/J_{w,0})_{baseline} - (J_w/J_{w,0})_{fouling} \right|}{(J_w/J_{w,0})_{baseline}} \times 100\% \quad (8)$$

236 where the $FD_{75\text{ mL}}$ was measured from the normalized baseline and fouling fluxes $(J_w/J_{w,0})_{baseline}$
 237 and $(J_w/J_{w,0})_{fouling}$, respectively. A lower bound of 0 for $FD_{75\text{ mL}}$ would indicate no occurrence
 238 of fouling; whereas, an upper bound of 100% would mean complete water permeability loss
 239 due to fouling.

240 Next, the fouled membranes were exposed to physical cleaning through circulation of
 241 DI water in both DS and FS channels for 1 h at a higher flow rate of 500 mL.min⁻¹. Lastly, the
 242 physically cleaned membranes were exposed to the conditions of baseline test to evaluate the
 243 flux recovery ratio (FRR) using Eq. 9:

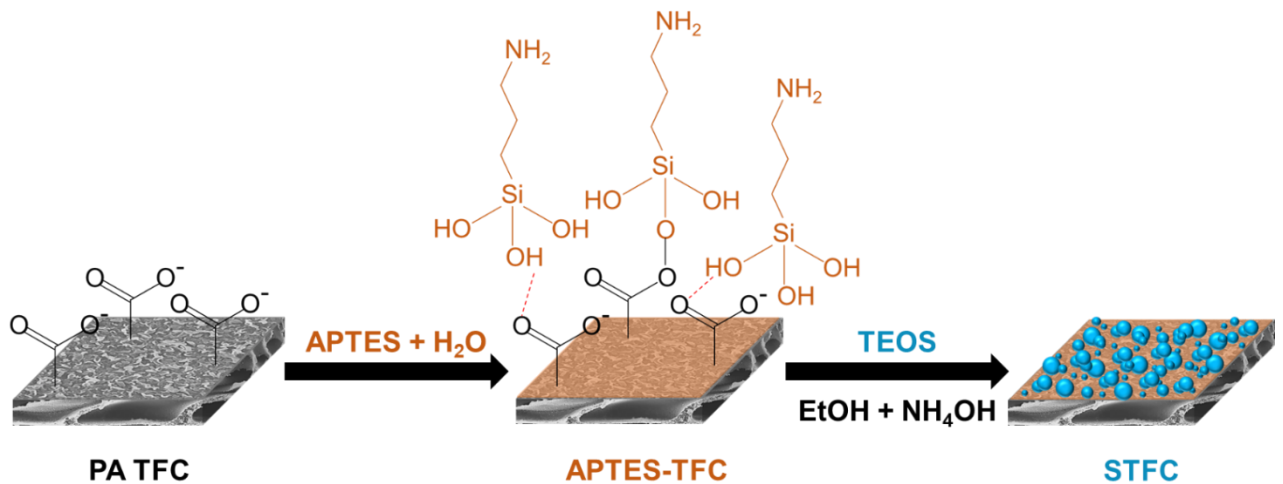
$$FRR = \frac{J_{w,0c}}{J_{w,0}} \quad (9)$$

244 where $J_{w,0}$ and $J_{w,0c}$ are the initial water fluxes of membranes before fouling and after cleaning,
 245 respectively.

246 **3 Results and discussion**

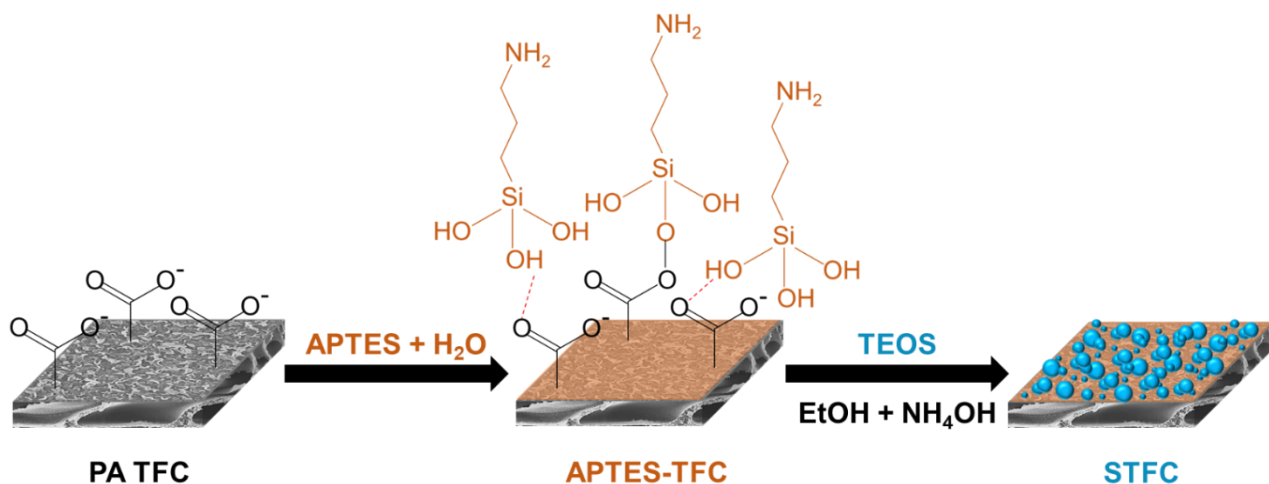
247 **3.1 Membrane surface properties**

248 The ultrathin silica layer was formed *in situ* on the PA TFC membrane surface, as
249 illustrated in



250

251 Figure 1. Firstly, the negatively charged TFC membrane was treated with positively
252 charged APTES, which was adsorbed on the membrane surface through attractive electrostatic
253 forces, hydrogen bonding and dehydration. The APTES then formed an aminosilane layer on
254 the PA surface through hydrolysis and self-condensation process and made the TFC membrane
255 surface positively charged (APTES-TFC) [38]. Secondly, the aminosilane layer of the APTES-
256 TFC membrane was exposed to a solution containing ethanol, ammonia and the negatively
257 charged TEOS. Due to the electrostatic attraction force, the TEOS monomers could attach on
258 the positively charged APTES-TFC membrane. Finally, the *in situ* silicification process
259 occurred via the hydrolysis–condensation process of the adsorbed TEOS monomers on the
260 APTES-TFC membrane surface; thus, ensuing the establishment of an ultrathin silica layer via
261 the nucleation and growth of nano-silica particles [39, 40].



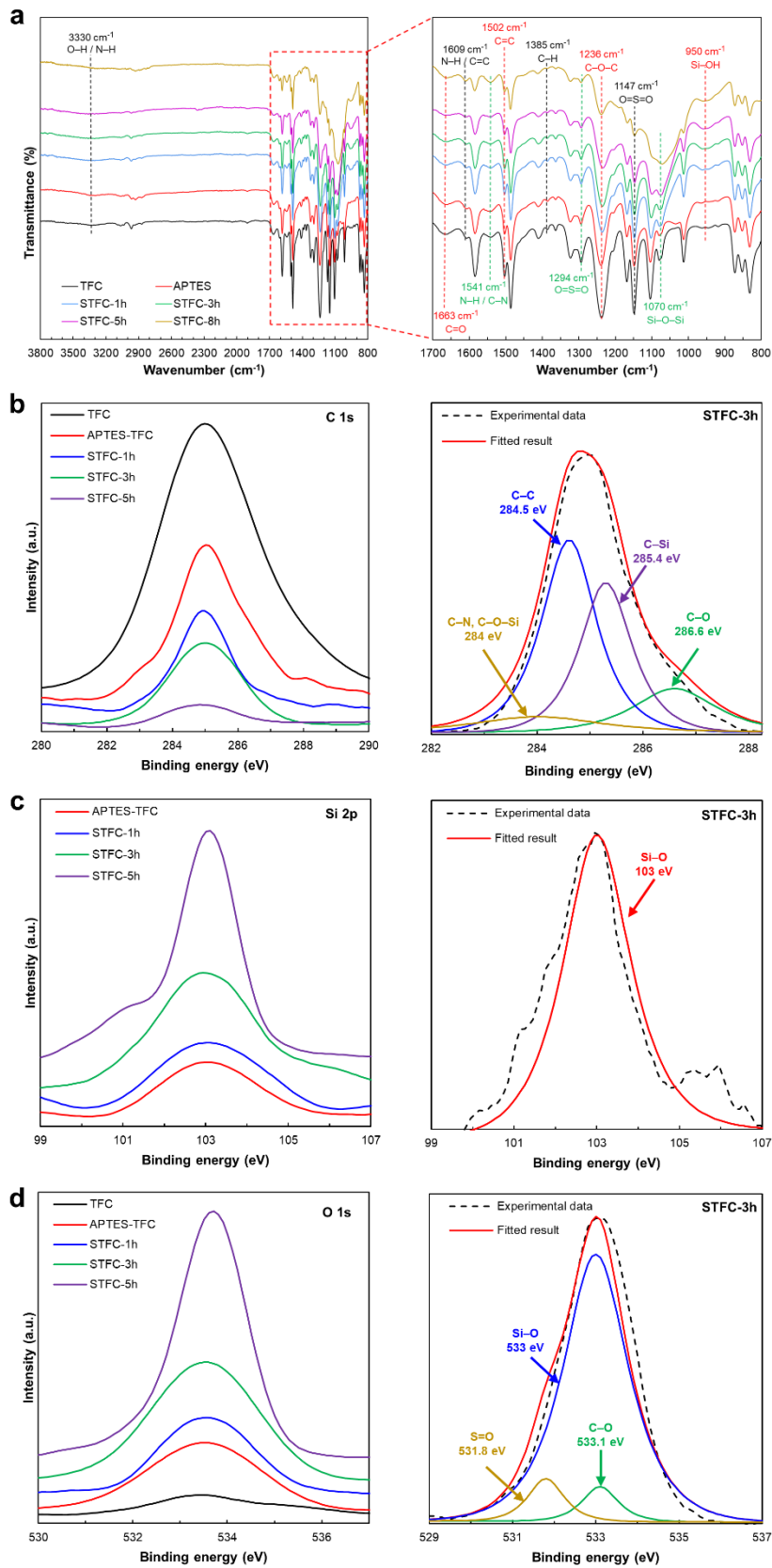
262

263 Figure 1: Schematic illustration of the procedure used to modify the PA TFC membrane surface
 264 via in situ silicification process. The blue spheres on the STFC membrane represent silica
 265 nanoparticles. APTES, H₂O, TEOS, EtOH and NH₄OH represent (3-aminopropyl)-
 266 triethoxysilane, water, tetraethoxysilane, ethanol and ammonium hydroxide, respectively.

267

268 The surface chemistries of the pristine TFC, APTES-TFC and resultant STFC
 269 membranes were examined using FTIR. As shown in Overall, both FTIR and XPS analysis
 270 confirm the effective growth of silica on the PA layer surface.

271



272

273

274

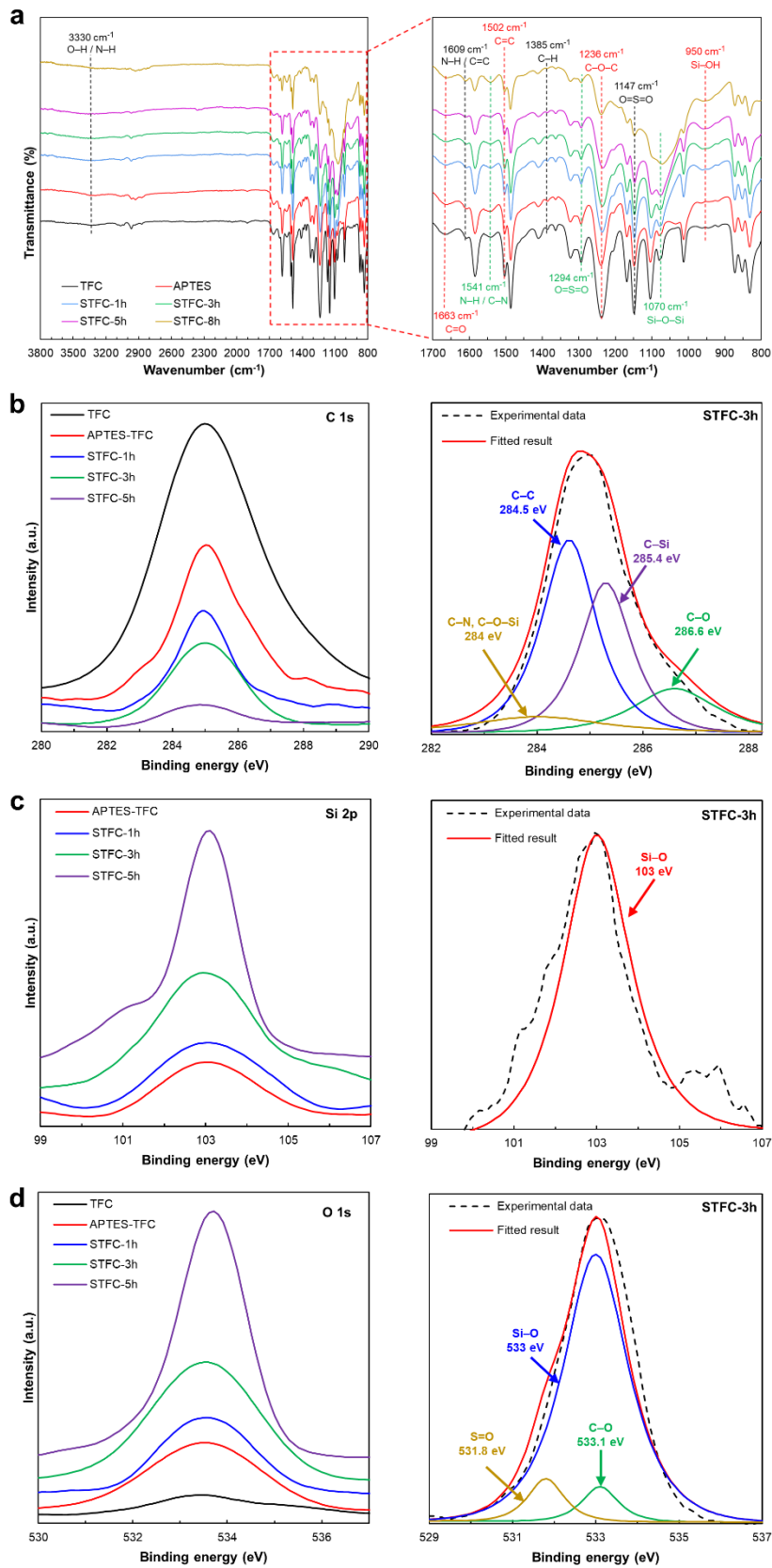
Figure 2a, the FTIR spectra of all the membranes revealed the characteristic peaks of polysulfone (PSf) at 1502 cm^{-1} (C=C aromatic ring in-plane scissoring vibration), 1385 cm^{-1}

275 (symmetric C–H deformation of C(CH₃)₂), 1236 cm⁻¹ (asymmetric C–O–C stretching vibration
276 of the aryl–O–aryl group), 1294 cm⁻¹ and 1147 cm⁻¹ (asymmetric and symmetric stretching
277 vibrations of the O=S=O bonds of PSf) [41, 42]. The membranes also exhibited the typical
278 peaks of PA at 1663 cm⁻¹ (amide I band), 1609 cm⁻¹ (aromatic amide band) and 1541 cm⁻¹
279 (amide II band, N–H in-plane bending vibration and C–N stretching of PA’s amide group) [36].
280 Since the STFC-1h, STFC-3h and STFC-5h membranes do not clearly show the silica-
281 associated peaks due to the small amount of silica on the membrane surface, the FTIR spectrum
282 of the STFC-8h membrane was also included to identify the peaks related to silica. The relative
283 intensity of the peaks at 1070 cm⁻¹ was higher for the APTES-TFC and STFC membranes
284 compared to the TFC membrane due to the Si–O–Si stretching vibration resulting from the
285 self-hydrolysis and condensation of APTES on the membrane surface throughout the self-
286 polymerization process [33]. The STFC membranes also revealed the characteristic Si–OH
287 stretching vibration peak of silica at 950 cm⁻¹ [43]. The relative intensity of this particular peak
288 augmented from STFC-1h to STFC-8h, indicating higher silica content obtained over longer
289 silicification time. Meanwhile, we also observed the decrease in relative intensities of the
290 characteristic PSf and PA FTIR bands. These results thus demonstrated the successful silica
291 deposition on the membrane surface. The broad band around 3330 cm⁻¹ ensues from the
292 overlapping peaks that are ascribed to the N–H and carboxyl group stretching of the PA, and
293 O–H stretching vibration of incomplete silanol group (Si–OH) condensation [44].

294 XPS measurements were also used to study the chemical composition alterations
295 resulting from the surface modification of the TFC membrane during *in situ* silicification
296 process. Both the qualitative and quantitative chemical analysis was performed with XPS at
297 the pristine and modified TFC membrane surfaces. The wide and narrow-scan XPS spectra
298 representing the carbon (C 1s), silicon (Si 2p), and oxygen (O 1s) elements for the pristine
299 TFC, APTES-TFC and STFC membranes prepared at various silicification times are presented

300 in Figure 2S1 and Figure 2b-d, respectively, while their surface elemental compositions are
301 summarized in Table 1. The large asymmetrical peak on the C 1s spectrum was deconvoluted
302 into four peaks; the peaks at 284.5 eV (the non-oxygenated carbon with sp^2 and sp^3
303 hybridization, C–C) and 286.6 eV (C–O) are associated to the PSf substrate [45], while the
304 peaks at 284 (C–O–Si, C–N) and 285.4 eV (C–Si) develop from APTES treatment on the
305 membrane surface [46]. The intensity of the C 1s peaks decreased at higher silicification
306 duration because of the formation of thicker silica layers (Figure 2b). The Si 2p XPS spectra
307 of the APTES-TFC and STFC membranes demonstrated a peak at 103 eV; thus, indicating the
308 formation of Si–O bonds after the APTES treatment and silicification process (Figure 2c) [47].
309 The deconvoluted XPS spectrum of the O 1s showed the presence of three additional peaks:
310 the C–O (533.1 eV) and S=O (531.8 eV) bands of the PSf substrate, and the Si–O peak (533
311 eV) from the silica coating (Figure 2d). The intensities of both the Si 2p and O 1s peaks were
312 observed to increase with increasing silicification duration due to the development of a denser
313 silica layer on the APTES-TFC membrane surface (Figure 2c and d). Consequently, the
314 elemental compositions of Si and O increased from 16.7% to 29%, and 29.3% to 43.3%,
315 respectively, while that of C decreased from 54.1% to 27.7% on increasing the silicification
316 duration from 1 h to 5 h (Table 1). Overall, both FTIR and XPS analysis confirm the effective
317 growth of silica on the PA layer surface.

318



319

320 Figure 2: (a) FTIR spectra, and narrow-scan XPS spectra of (b) C, (c) Si, and (d) O elements of
 321 pristine and modified TFC membranes prepared at various silicification durations.

322

323 Table 1: Surface elemental compositions of the pristine and modified TFC membranes.

Membrane	C (%)	O (%)	Si (%)
TFC	85.78	14.22	0.00
APTES-TFC	70.66	20.76	8.58
STFC-1h	54.05	29.26	16.69
STFC-3h	40.88	38.16	20.97
STFC-5h	27.69	43.33	28.98

324

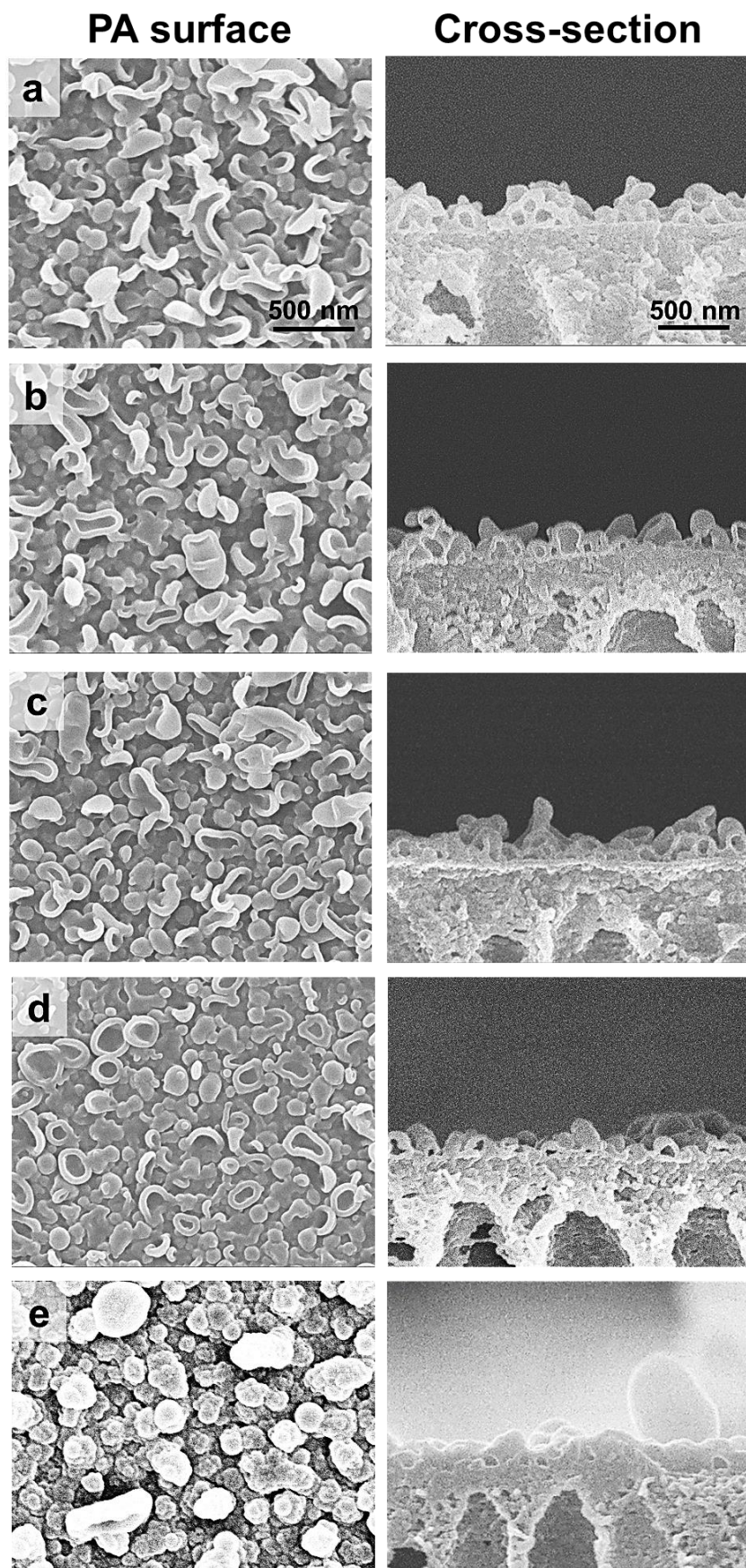
325 The surface and cross-section morphologies of the pristine and ultrathin silica coated
 326 PA TFC membranes were systematically investigated via SEM (Figure 3) and AFM (Figure 5)
 327 characterizations. The pristine TFC membrane demonstrated the characteristic ridge-and-
 328 valley structure of the PA layer (Figure 3a); thus confirming the successful completion of IP
 329 process on the PSf substrate. The APTES-TFC membrane demonstrated similar morphology
 330 (Figure 3b) and roughness (Figure 5b) as that of the TFC membrane (Figure 3a and Figure 5a),
 331 which confirms that the APTES treatment had no significant influence on the morphology of
 332 the PA layer (Figure 3b, Figure 5b). However, the SEM images of the STFC-1h, STFC-3h and
 333 STFC-5h surfaces (Figure 3c-d) revealed more distinct morphologies with uniform deposition
 334 of silica nanoparticles, which implies that the *in situ* silicification process occurred
 335 successfully on the PA layer surface.

336 During the first hour of the silicification process, the hydrolysis-condensation reactions
 337 of the APTES and TEOS formed silica nuclei on the surface of STFC-1h as can be observed
 338 from Figure 3c. By prolonging the silicification time to 3 h, the silica nuclei grew bigger to
 339 form a more continuous silica layer on the STFC-3h surface (Figure 3d). However, the
 340 deposited silica nanoparticles were barely visible on the SEM cross-section images (Figure 3c-
 341 d, right images), which suggests that the growth of ultrathin silica layer only influences the

342 membrane surface chemistry without significantly changing the membrane morphology.
343 However, on further increasing the silicification time to 5 h, we observed a denser and thicker
344 interconnected layer of silica clusters that mostly covered the PA surface as demonstrated by
345 the surface and cross-section SEM images of the STFC-5h membrane (Figure 3e). The larger-
346 sized silica nanoparticles emerged due to collision and coagulation of the silica nuclei that were
347 continuously in random motion [33]. These results confirmed that the size of silica particles
348 and the thickness of the silica layer on the surface of the membrane could be easily adjusted
349 through varying the silicification time.

350

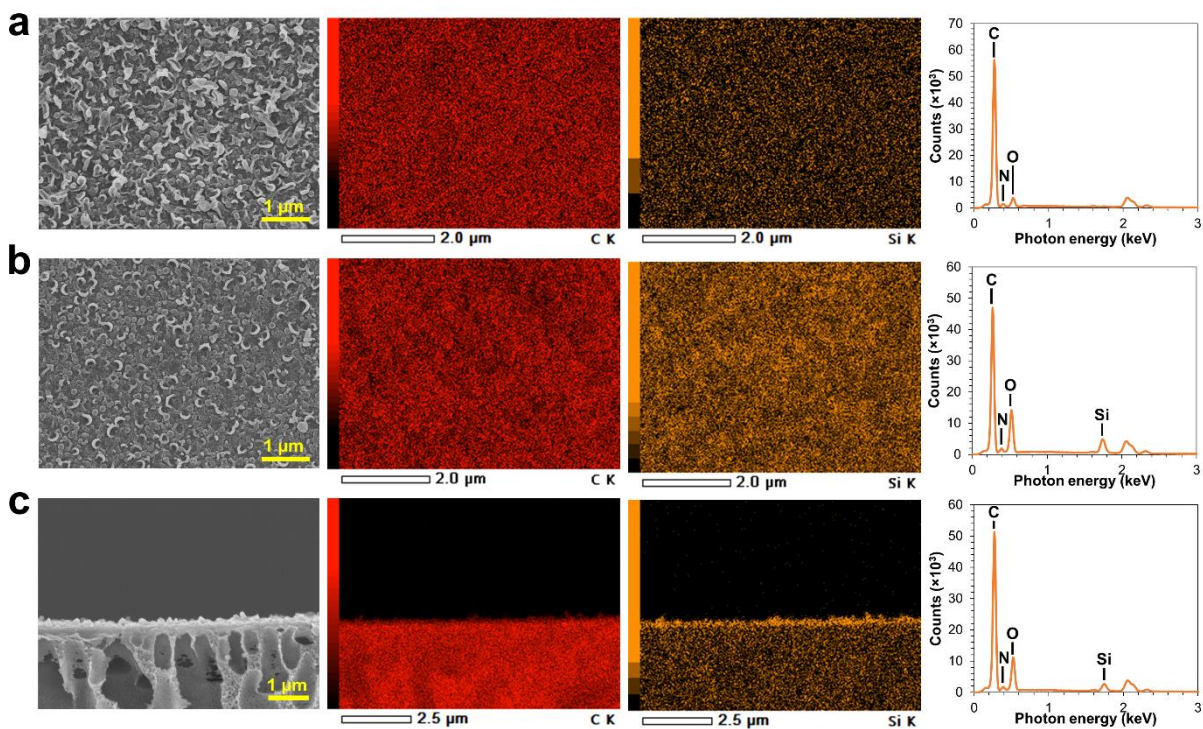
351



352

353 Figure 3: SEM images showing PA TFC membrane top surface and cross-section morphologies
 354 of (a) pristine TFC, (b) APTES-TFC, (c) STFC-1h, (d) STFC-3h, and (e) STFC-5h membranes.

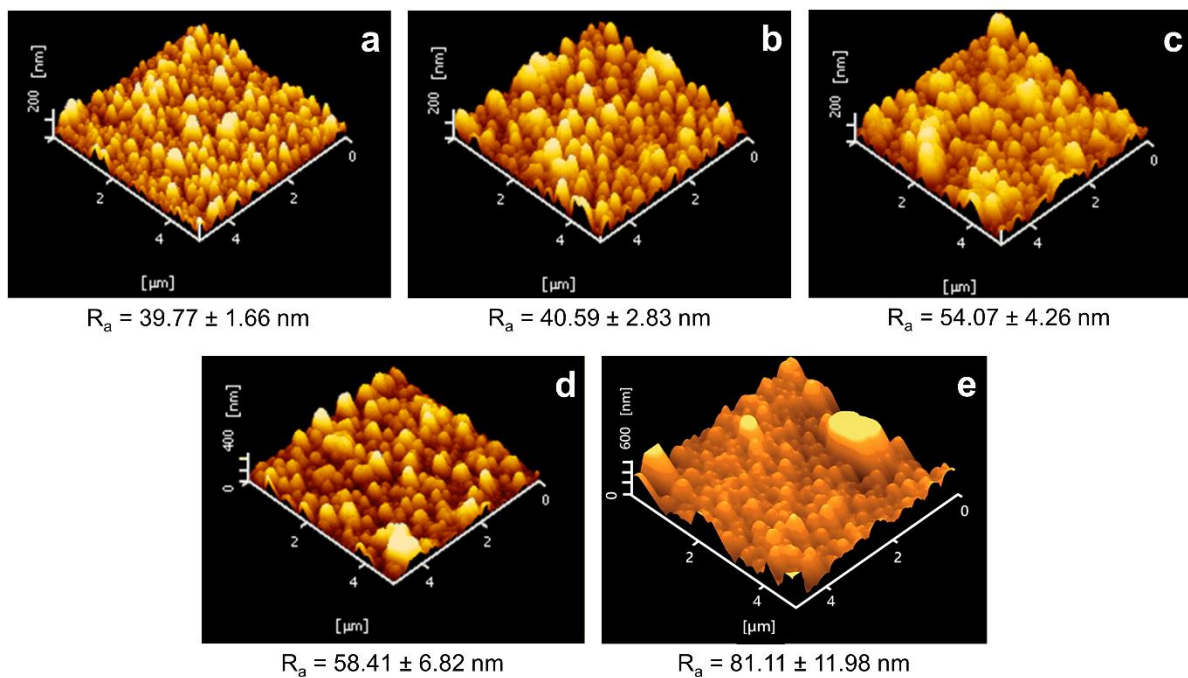
355 The EDS mapping and spectra of the pristine TFC and silica-modified STFC
 356 membranes are presented in Figure 4. It can be observed from the EDS elemental mapping
 357 results of Si and O that silica (SiO_2) is uniformly distributed on the surface of the STFC
 358 membrane. Since silica is not grown on the surface of the pristine TFC membrane, the Si peak
 359 is missing from its EDS spectrum (Figure 4a). In contrast, the EDS spectrum of the STFC
 360 membrane showed more intense Si and O peaks comparatively due to silica deposition on its
 361 surface (Figure 4b). The EDS mapping results of the STFC membrane's cross-section SEM
 362 image showed a thin layer of Si on its surface (Figure 4c), which further confirmed that a thin
 363 silica layer was mainly deposited on the PA layer surface without obvious intrusion into the
 364 porous PSf substrate.



365
 366 Figure 4: SEM, EDS mapping and EDS spectra of (a) pristine TFC membrane top surface, (b)
 367 silica coated STFC membrane top surface and (c) silica coated STFC membrane cross-section.
 368 Red and orange dots on EDS mapping indicate signals of carbon (C) and silica (Si),
 369 respectively.

370

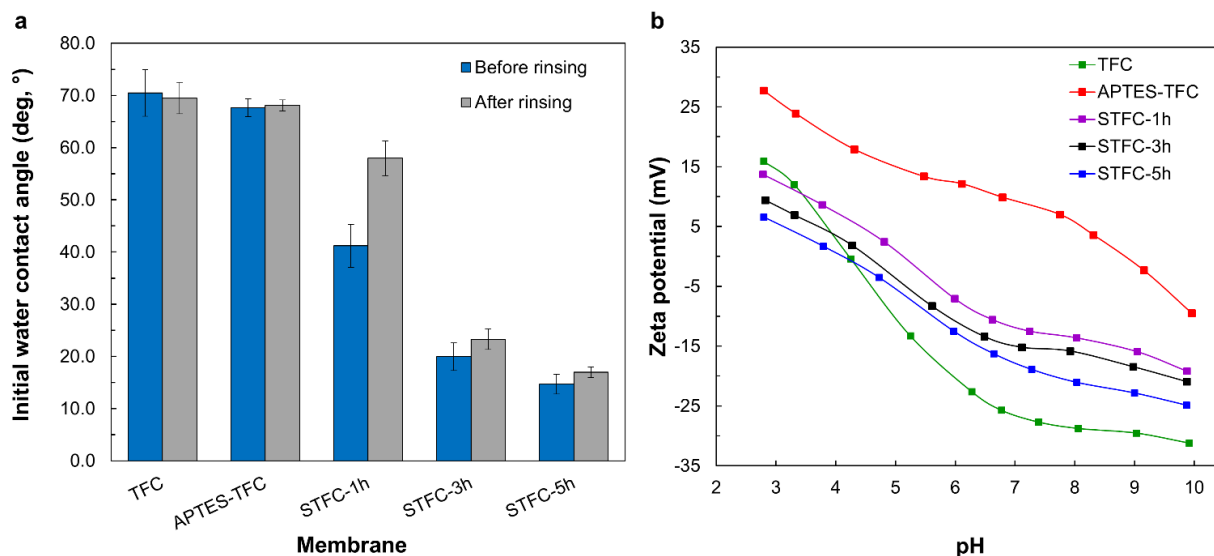
371 As evident from AFM topography results, the surface of the STFC membranes became
372 rougher as the silicification process duration was increased from 1 h to 5 h (Figure 5). The
373 average surface roughness (R_a) of the silica-modified PA TFC membranes increased from
374 54.07 nm for STFC-1h, to 58.41 nm for STFC-3h, and 81.11 nm for STFC-5h membranes due
375 to the formation of larger silica nanoparticle clusters on the PA surface (Figure 5c-e). The
376 pristine TFC and APTES-TFC membranes demonstrated comparatively smoother surfaces
377 with near identical R_a values of 39.77 and 40.59 nm, respectively (Figure 5a and b). This
378 observation further confirms that the APTES treatment did not considerably modify the
379 morphology of the TFC membrane but primarily modified its surface chemistry, which will be
380 verified later from the contact angle and surface zeta potential measurements.



382 Figure 5: AFM topography images representing membrane surface roughness of (a) pristine
383 TFC, (b) APTES-TFC, (c) STFC-1h, (d) STFC-3h, and (e) STFC-5h membranes. Error bars
384 for membrane surface roughness represent one standard error obtained from at least 3
385 membrane samples for each condition.

386

387 The membrane surface wettability of the pristine TFC, APTES-TFC and silica coated
 388 STFC membranes was determined from the initial water contact angles measured on their
 389 surfaces. As can be observed from



390
 391 Figure 6a, the pristine TFC membrane possessed the least hydrophilic surface before
 392 water rinsing with a contact angle of 71°. The TFC membrane's surface hydrophilicity
 393 improved slightly after 16 h of APTES treatment (APTES-TFC) and exhibited a water contact
 394 angle of 68°. However, the silica coated STFC membranes displayed a significant improvement
 395 in wettability with lower water contact angles. Specifically, the water contact angles declined
 396 from 41° for STFC-1h to 15° for STFC-5h when the silicification process duration increased
 397 from 1 h to 5 h due to more silica deposition on the membrane surface. The observed trend in
 398 membrane hydrophilicity suggests that the silica coating can improve the membrane
 399 hydrophilicity as it comprises of a considerable quantity of hydrophilic silanol and related
 400 hydroxyl groups.

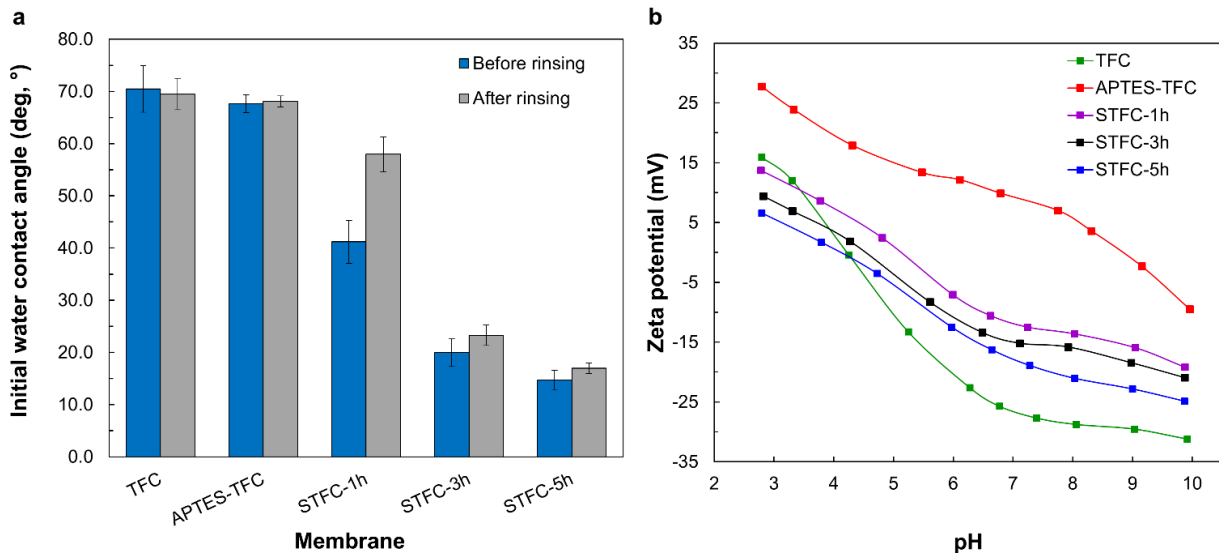
401 To determine the stability of the silica layer on the STFC membranes, the membranes
 402 were subjected to rinsing at higher cross-flow velocity of 12 cm.s⁻¹ for 72 h at room temperature
 403 using DI water. As expected, the initial water contact angle of the TFC membrane did not
 404 change after rinsing (Figure 6a). The APTES-TFC membrane also revealed similar water

405 contact angles before and after rinsing, which confirmed the stability of the aminosilane layer
406 under the applied high shear operating conditions. The hydrophilicity of the STFC-1h
407 membrane, on the other hand, significantly declined with the water contact angle increasing
408 from 41° to 58° after high shear rinsing possibly because of the weak attachment of silica
409 particles to the membrane surface. The STFC-3h and STFC-5h membranes also exhibited
410 reduced hydrophilicity after DI water rinsing, but their water contact angles increased only by
411 3.3° and 2.3°, respectively, which is insignificant compared to that of the STFC-1h membrane.
412 Hence, it can be resolved that the stability of the silica layer increased at higher silicification
413 time.

414 The surface charge of the TFC, APTES-TFC and silica-modified STFC membranes are
415 shown in terms of the zeta potential measurements over a pH range of 3 to 10, as presented in
416 Figure 6b. The pristine TFC membrane's was observed to be positively charged at pH < 3.5
417 due to the protonation of the PA layer's pendant amino groups. At pH > 3.5, the pristine TFC
418 membrane exhibited a negatively charged surface owing to the deprotonation of the PA layer's
419 carboxyl and amino groups [48]. The negatively charged surface of the TFC membrane
420 facilitated adsorption of positively charged APTES on its surface via attractive electrostatic
421 forces, in addition to hydrogen bonding. As revealed by Figure 6b, the aminosilane layer
422 formed on the PA layer from hydrolysis and self-condensation of APTES rendered the TFC
423 membrane surface positively charged (APTES-TFC), which further assisted in adsorption of
424 negatively charged TEOS via electrostatic interaction to form an ultrathin silica coating
425 through *in situ* silicification via hydrolysis-condensation process [38].

426 The preparation of silica layer on PA surface subsequently reversed the membrane
427 surface charge from positive (APTES-TFC) to negative (STFC-1h, STFC-3h and STFC-5h)
428 [33, 49]. In summary, the TFC membrane revealed the most negatively charged surface,
429 comparatively, because of the presence of abundant carboxyl groups. In contrast, the surface

430 negative charge of the STFC membranes was lower compared to the pristine membrane owing
 431 to the silica layer's shielding effect that reduced the exposure of PA carboxyl groups [50].
 432 Moreover, the zeta potentials for the STFC membranes progressively became more negative
 433 as the silicification duration increased from 1 h (STFC-1h) to 5 h (STFC-5h) due to formation
 434 of more silica particles that contained abundant negatively charged hydroxyl groups [51].



435 Figure 6: (a) Initial water contact angle measurements of the pristine and modified TFC
 436 membranes before and after rinsing with DI water for 72 h at a co-current cross-flow velocity
 437 of 12 cm.s⁻¹; (b) surface zeta potential measurements of the pristine and modified TFC
 438 membranes. Error bars for initial water contact angle measurements represent one standard
 439 error obtained from at least 7 measurements for each membrane sample.
 440

441

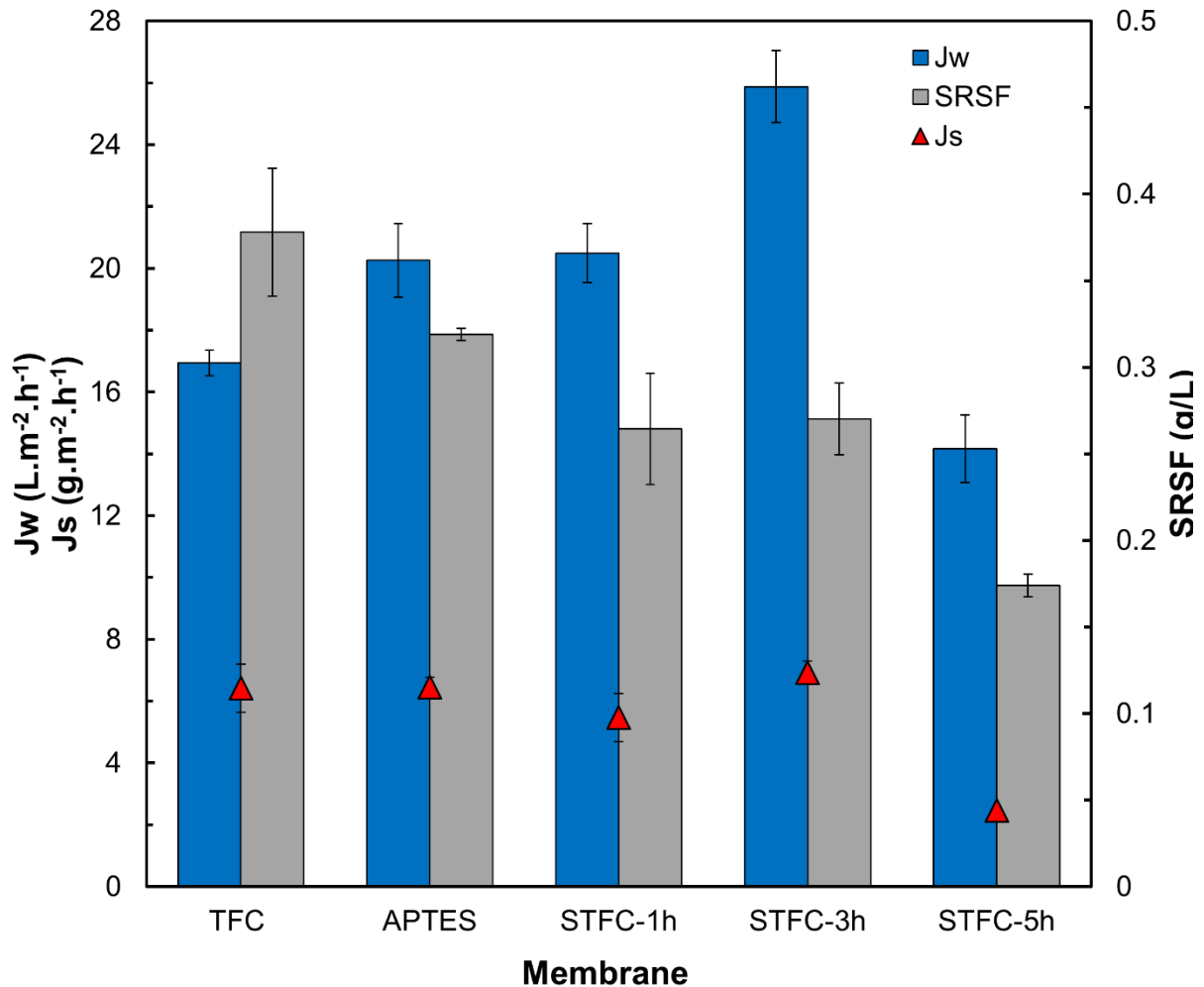
442 3.2 FO membrane performance

443 The FO performance of the pristine TFC, APTES-TFC and STFC membranes were
 444 determined in AL-FS orientation using 1 M NaCl as DS and DI water as FS. The reverse solute
 445 flux (J_s), water flux (J_w) and specific reverse solute flux ($SRSF$) across the prepared membranes
 446 are presented in Figure 7. Due to the improved surface hydrophilicity of the APTES-TFC
 447 membrane, it showed a higher J_w (20 L.m⁻².h⁻¹) compared to the pristine TFC membrane (17
 448 L.m⁻².h⁻¹). The J_s of the APTES-TFC membrane, however, remained similar as that of the TFC
 449 membrane (~6.4 g.m⁻².h⁻¹), which confirmed that 16 h of APTES treatment altered the

450 membrane surface properties without impairing the PA layer. The STFC-1h showed a similar
451 J_w as that of the APTES-TFC membrane possibly due to formation of an unstable silica coating
452 that partially washed off during the test as observed from the increase in its water contact angle
453 measurements after rinsing (Figure 6a). The J_w of the STFC-1h membrane interestingly
454 decreased slightly ($5.5 \text{ g.m}^{-2}.\text{h}^{-1}$), probably due to the negatively charged membrane surface
455 repelling the DS ions away from it. Owing to the improved stability of the silica layer on the
456 STFC-3h membrane, as evident from its water contact angle results (Figure 6a), it demonstrated
457 the highest J_w of $26 \text{ L.m}^{-2}.\text{h}^{-1}$ with a small increase in the J_s ($6.9 \text{ g.m}^{-2}.\text{h}^{-1}$) as a result of the
458 permeability-selectivity trade-off relationship. Both the J_w and J_s of the STFC-5h membrane
459 ($14 \text{ L.m}^{-2}.\text{h}^{-1}$ and $2.5 \text{ g.m}^{-2}.\text{h}^{-1}$, respectively) were the lowest compared to other membranes
460 because of the increased hydraulic resistance from the dense silica layer formation that coated
461 nearly the entire PA layer surface, as observed earlier from the SEM images (Figure 3e).
462 Although STFC-5h membrane revealed the most hydrophilic surface, however, a thicker silica
463 layer negatively impacted the J_w as a consequence of the additional hydraulic resistance. The
464 dense silica layer, however, improved the selectivity of the membrane by both electrostatic
465 repulsion and the size exclusion effect to draw solute; consequently, diminishing the J_s the
466 STFC-5h membrane.

467 The *SRSF* is an imperative parameter in the FO process specifying the selectivity of the
468 FO membranes, and a lower *SRSF* value is preferable as it denoted a more selective
469 membrane. As shown in Figure 7, APTES treatment of the TFC membrane reduced its *SRSF*
470 value by 16% in comparison to the TFC membrane. Likewise, the modified TFC membranes
471 with silica layer attained lower *SRSF* values in comparison to the TFC membrane owing to
472 their relatively higher J_w with similar J_s resulting from the increased membrane hydrophilicity
473 and surface negative-charge. Specifically, the highest *SRSF* value of 0.38 g.L^{-1} was observed
474 for the TFC membrane because of the looser pore structure of its PA layer, which facilitated

475 relatively more solute particles to move to the FS from the DS. The STFC-1h (0.26 g.L⁻¹) and
 476 STFC-3h (0.27 g.L⁻¹) showed comparable SRSF values, but the SRSF of STFC-5h (0.17 g.L⁻¹)
 477 ¹) was significantly smaller because of the augmented resistance from the dense silica layer.
 478 The STFC-3h was selected as the most favourable membrane as it revealed the highest J_w in
 479 comparison to other silica-modified TFC membranes without deteriorating its selectivity.



480

481 Figure 7: FO performance of the pristine and modified TFC membranes with 1 M NaCl as DS
 482 and DI water as FS in AL-FS arrangement at a co-current cross-flow velocity of 12 cm.s⁻¹.
 483 Error bars for membrane surface roughness represent one standard error obtained from at least
 484 3 membrane samples for each condition.

485

486 The intrinsic transport properties of the pristine and modified TFC membranes were
 487 determined from the pure water permeability coefficient (A), solute permeability coefficient
 488 (B), and intrinsic membrane selectivity ratio (B/A) as listed in Table 2. The APTES-TFC

489 membrane with the aminosilane layer, and the silica coated STFC-1h and STFC-3h membranes
 490 demonstrated higher A values (2.14, 2.18 and 2.46 $\text{L}\cdot\text{m}^{-2}\cdot\text{h}^{-1}\cdot\text{bar}^{-1}$, respectively) in comparison
 491 with the pristine TFC membrane (2.08 $\text{L}\cdot\text{m}^{-2}\cdot\text{h}^{-1}\cdot\text{bar}^{-1}$) due to their improved surface
 492 hydrophilicity. The B values of the modified membranes showed a similar trend as that of the
 493 membrane J_s during the FO performance due to the same reasons discussed above. However,
 494 the STFC-5h membrane displayed the lowest A (1.78 $\text{L}\cdot\text{m}^{-2}\cdot\text{h}^{-1}\cdot\text{bar}^{-1}$) and B (0.43 $\text{L}\cdot\text{m}^{-2}\cdot\text{h}^{-1}$)
 495 value, compared to the pristine and modified TFC membranes, due to the development of a
 496 dense silica layer on its surface that reduced its water permeability and increased the draw
 497 solute selectivity by raising the hydraulic resistance across it. The least selective TFC
 498 membrane showed the biggest B/A ratio of 0.36 bar; whereas, the STFC-5h was found to be
 499 the most selective with a smallest B/A ratio of 0.24 bar. Both STFC-1h and STFC-3h
 500 membranes exhibited similar selectivity with B/A ratios of 0.29 bar and 0.31 bar, respectively.
 501 The intrinsic transport parameters are in good agreement with the FO performance of the
 502 membranes presented in Figure 7d, and validated that the membrane performance could be
 503 adjusted by tuning the silicification time.

504 Table 2: Intrinsic transport parameters of pristine and modified TFC FO membranes. Error bars
 505 represent one standard error obtained from at least 3 membrane samples for each condition.

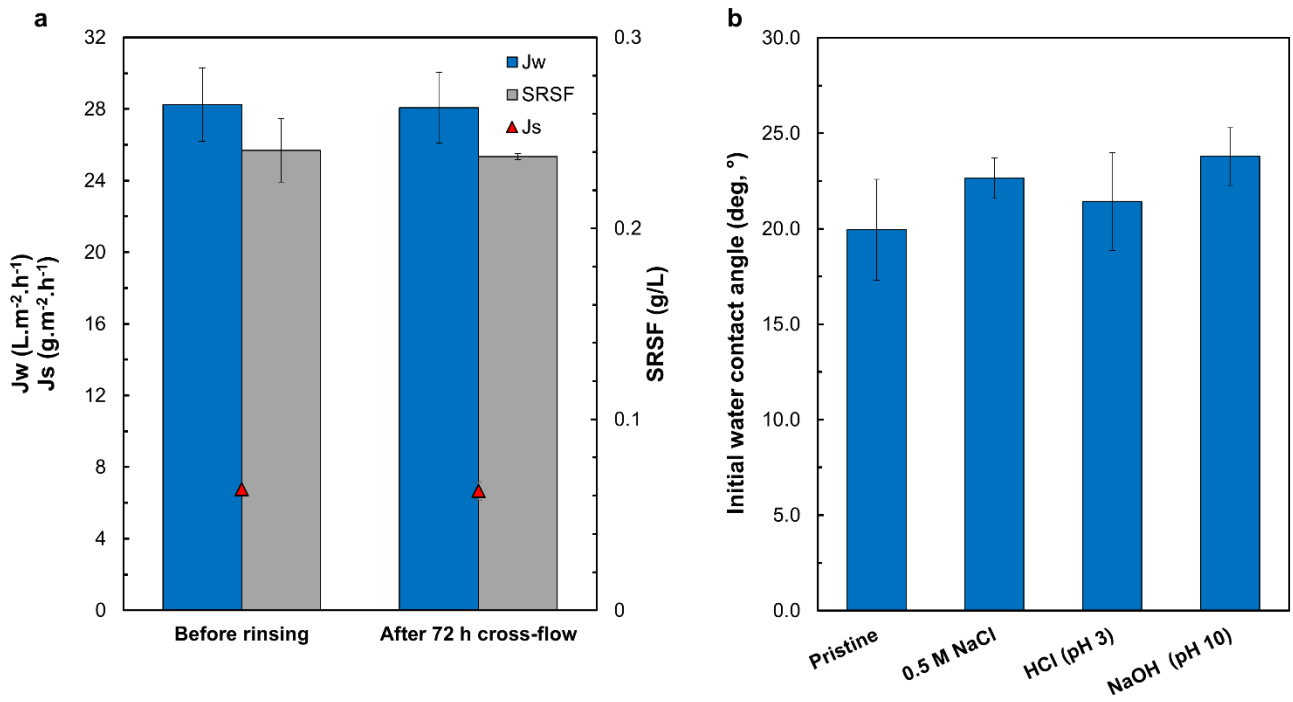
Membrane	A ($\text{L}\cdot\text{m}^{-2}\cdot\text{h}^{-1}\cdot\text{bar}^{-1}$)	B ($\text{L}\cdot\text{m}^{-2}\cdot\text{h}^{-1}$)	B/A (bar)
TFC	2.08 ± 0.26	0.75 ± 0.06	0.36 ± 0.013
APTES-TFC	2.14 ± 0.19	0.73 ± 0.10	0.34 ± 0.014
STFC-1h	2.18 ± 0.09	0.63 ± 0.04	0.29 ± 0.005
STFC-3h	2.46 ± 0.18	0.76 ± 0.07	0.31 ± 0.005
STFC-5h	1.78 ± 0.17	0.43 ± 0.02	0.24 ± 0.010

506

507 3.3 Membrane stability

508 The durability and stability of the membrane coating are crucial factors in evaluating
509 the potential of scaling-up for practical applications. Therefore, the optimal STFC-3h
510 membrane was subjected to a high co-current cross-flow velocity shear of $12 \text{ cm}\cdot\text{s}^{-1}$ operated
511 for 72 h using DI water to assess the mechanical stability of the silica-coating on the TFC
512 membrane surface. As presented in Figure 8a, the STFC-3h membrane revealed identical FO
513 performance both before and after intense rinsing with DI water; thus, demonstrating that the
514 silica coating remained mechanically stable over the long-term cross-flow rinsing process. The
515 FO test results are in good conformity with the contact angle measurements, as discussed earlier
516 (Figure 6a).

517 The STFC-3h membrane was also treated with salt, acid and base to further investigate
518 its chemical stability under various conditions, as shown in Figure 8b. It was found that STFC-
519 3h membrane exhibited only 2.7° increase in water contact angle after exposing to a 0.5 M
520 NaCl solution by constant shaking for 72 h, suggesting an excellent chemical stability.
521 Similarly, the treatment of STFC-3h membrane with HCl and NaOH showed only a slight rise
522 in water contact angle by 1.4° and 3.8° , respectively, which is within the measurement error
523 range. These results proved that the silica layer on the STFC-3h membrane surface remained
524 stable under various chemical exposures, which could be attributed to the exceptional adhesion
525 force between the silica and aminosilane layers via the stable, covalent Si–O–Si bonds. These
526 results also suggest that the STFC-3h membrane can be suitably applied under harsh
527 environment.



528

529 Figure 8: a) FO performance of STFC-3h membrane before and after rinsing with DI water for
 530 72 h at a co-current cross-flow velocity of 12 cm.s⁻¹. The membranes were tested in AL-FS
 531 arrangement with 1 M NaCl as DS and DI water as FS at a co-current cross-flow velocity of
 532 12 cm.s⁻¹. b) Initial water contact angle measurements of the STFC-3h membrane before and
 533 after its exposure to the salt solution (0.5 M NaCl), acid (HCl, pH 3) and base (NaOH, pH 10)
 534 for 72 h at 70 rpm. Error bars for FO performance (initial water contact angle measurements)
 535 represent one standard error obtained from at least 2 membrane samples (5 random positions)
 536 for each condition.

537

538 3.4 Antifouling properties

539 The antifouling properties of the pristine TFC and STFC-3h membranes were examined
 540 using accelerated fouling experiments using different organic foulants (BSA, HA and SA), where
 541 the foulant dosage in the FS was maintained at 1 g.L⁻¹. Both BSA and SA were selected to exemplify
 542 the higher molecular weight compounds present in wastewaters and surface waters; while, the HA
 543 was chosen to demonstrate the effect of hydrophobic characteristics of the organic matter on the
 544 membrane fouling propensity. The normalized flux decline corresponding to 75 mL of permeate
 545 volume (FD_{75mL}) against different organic foulants is presented in Figure 9. As can be observed, the
 546 STFC-3h membrane showed a suggestively lower FD_{75mL} compared to the TFC membrane with all
 547 the foulants, indicating that surface modification of PA layer with silica layer can improve

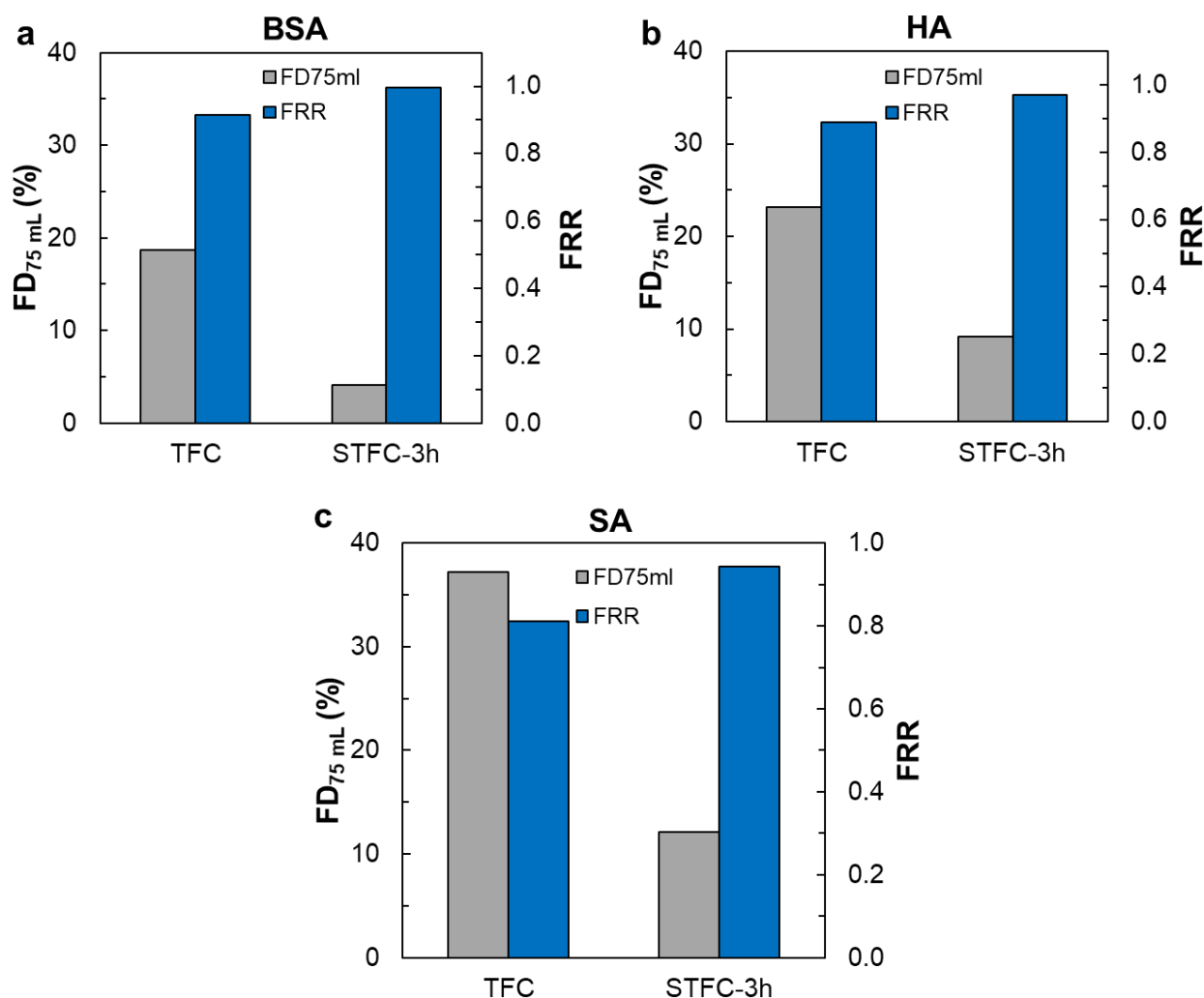
548 antifouling properties of the membrane as a result of their improved hydrophilicity. The TFC
549 membrane's poor antifouling property could be attributed to the development of a dense foulant
550 layer on its surface owing to the strong interaction forces between its more hydrophobic surface and
551 the organic foulants.

552 The flux decline in both TFC and STFC-3h membranes with BSA and HA was considerably
553 lower than that with SA. For instance, STFC-3h (TFC) revealed a FD_{75mL} of 4.2% and 9.1% (18.7%
554 and 23.2%) with BSA and HA, respectively, which is relatively lower than a FD_{75mL} of 12.14%
555 (37.2%) obtained with SA. These results indicate that both BSA and HA do not adhere to the
556 membrane surfaces easily compared to SA, which resulted in a lower flux decline. The more serious
557 SA fouling could be ascribed to the Ca^{2+} bridging effect between the ions and the abundant
558 carboxylic functional forming a highly cross-linked foulant layer on the membrane surface [36, 52].
559 Since the BSA molecules contain only a low amount of carboxylic groups, the presence of Ca^{2+} in
560 the FS has minor influence on the BSA fouling tendency [53].

561 In comparison to the TFC membrane, the STFC-3h membrane exhibited a suggestively
562 better antifouling property to all the foulants owing to the existence of fewer carboxyl groups on its
563 surface. The *in situ* APTES treatment and silicification process on the PA layer partially occupied
564 the carboxyl groups on the PA layer, which effectively diminished the inter-adhesion between
565 foulants and the membrane surface; thus, leading to the lower membrane fouling potential. The
566 hydrophilic silica coating on the STFC-3h membrane also mitigated fouling by forming a water
567 obstruction amid the hydrophobic foulants and the membrane surface that weakened the interfacial
568 interaction between them [21, 54]. Overall, the fouling test results confirm that the membrane
569 surface properties can radically impact the membrane fouling behaviour, and that weakening the
570 foulant-membrane interfacial interaction could reduce foulant accumulation onto membrane
571 surface; thereby, reducing the membrane flux decline.

572 After the end of the fouling tests, the membranes were exposed to simple physical cleaning
573 with DI water for 1 h at a higher cross-flow velocity of 0.5 L.min⁻¹ and tested under the initial
574 baseline conditions to assess their FRR. As presented in Figure 9, the STFC-3h membrane achieved
575 a greater FRR than that of the TFC membrane under all conditions due to its more hydrophilic
576 surface, which weakened the foulant–membrane and foulant–foulant interactions. Both the TFC and
577 STFC-3h membranes revealed increased normalized flux after the physical cleaning, which
578 indicates the fouling reversibility of the membranes up to a certain extent. The FRR of the TFC
579 membrane was 91.4% and 88.7%, whereas, that of STFC-3h membrane was 99.6% and 96.9% after
580 BSA and HA fouling, respectively. In the case of SA fouling, the TFC membrane attained a small
581 FRR of 81.2%, suggesting substantial irreversible fouling because of strong adhesion of SA layer
582 on the membrane surface. However, the STFC-3h membrane exhibited a comparatively higher flux
583 recovery of 94.4% after SA fouling due to its hydrophilic surface that contained less carboxylic
584 functional groups and foulant adhesive sites, which allowed a greater extent of foulant removal from
585 its surface. Consequently, the improved antifouling property of the STFC-3h membrane diminished
586 the foulant-membrane interaction by facilitating the development of a loosely adhered foulant layer
587 that could be effortlessly eradicated by simple hydraulic rinsing process. It could be concluded from
588 the fouling tests that the BSA and HA fouling is more reversible than the SA fouling, and that the
589 membrane cleaning efficiency is governed by the severity of foulant–foulant and foulant-membrane
590 interactions.

591



592

593 Figure 9: The normalized flux decline ($FD_{75\text{mL}}$) during the accelerated fouling test with $1\text{g}\cdot\text{L}^{-1}$
 594 a) BSA, b) HA, and c) SA, and the flux recovery ratio (FRR) after physical cleaning of the
 595 pristine TFC and modified STFC-3h membranes. Operating conditions: Initial baseline water
 596 flux ($J_{w,0}$), $\sim 20\text{ L}\cdot\text{m}^{-2}\cdot\text{h}^{-1}$; membrane orientation, AL-FS; DS, 0.5-2 M NaCl; foulants, 1 mM
 597 calcium chloride and $1\text{g}\cdot\text{L}^{-1}$ BSA/HA/SA; flow rate (baseline and fouling test), $0.25\text{ L}\cdot\text{min}^{-1}$;
 598 flow rate (physical cleaning), $0.5\text{ L}\cdot\text{min}^{-1}$.

599

600 4 Conclusions

601 In this work, surface modification of PA TFC membranes was explored by varying the
 602 duration of *in situ* silicification process to form an ultrathin silica layer on the PA membrane
 603 surface. The density of silica coating on the PA layer surface and its surface wettability and
 604 surface charge increased with the increase of silicification duration; however, 3 h was observed
 605 to be optimum duration beyond which the water transport resistance of the membrane

606 increased. This optimum membrane (STFC-3h) demonstrated the best silica coating stability
607 and FO process performances with the highest water enhancement of 53% while retaining
608 membrane selectivity in AL-FS orientation in comparison to the pristine TFC membrane. The
609 improved FO performance could be ascribed to the enhanced surface hydrophilicity resulting
610 from the hydrophilic silica coating. The inorganic silica coating on the STFC-3h membrane
611 surface also showed good mechanical stability and thermal stability when subjected high cross-
612 flow shear rinsing (with DI water) for 72 h and also when exposed to high salinity, acidic and
613 basic solutions. Moreover, the hydrophilic STFC-3h membrane revealed improved antifouling
614 property and flux recovery rate than that of the TFC membrane when exposed to BSA, HA and
615 SA fouling by reducing the foulant-membrane and foulant-foulant interactions. Overall, the
616 facile *in situ* silicification technique for membrane PA surface modification shown in this study
617 opens up a promising pathway to augment the FO performance and antifouling property of the
618 PA TFC membranes.

619 **Acknowledgement**

620 The research reported in this paper was supported by the ARC Industrial Transformation
621 Research Hub (IH170100009) and the King Abdullah University of Science and Technology
622 (KAUST), Saudi Arabia through the Competitive Research Grant Program – CRG2017
623 (CRG6), Grant # URF/1/3404-01.

624

625 **References**

- 626 [1] V.H. Tran, S. Lim, D.S. Han, N. Pathak, N. Akther, S. Phuntsho, H. Park, H.K. Shon,
627 Efficient fouling control using outer-selective hollow fiber thin-film composite membranes for
628 osmotic membrane bioreactor applications, *Bioresource Technology*, 282 (2019) 9-17.
- 629 [2] N. Akther, S. Daer, S.W. Hasan, Effect of flow rate, draw solution concentration and
630 temperature on the performance of TFC FO membrane, and the potential use of RO reject brine
631 as a draw solution in FO–RO hybrid systems, *Desalination and Water Treatment*, 136 (2018)
632 65-71.
- 633 [3] J. Zhang, Q. She, V.W.C. Chang, C.Y. Tang, R.D. Webster, Mining Nutrients (N, K, P)
634 from Urban Source-Separated Urine by Forward Osmosis Dewatering, *Environmental Science
635 & Technology*, 48 (2014) 3386-3394.
- 636 [4] V. Sant’Anna, L.D.F. Marczak, I.C. Tessaro, Membrane concentration of liquid foods by
637 forward osmosis: Process and quality view, *Journal of Food Engineering*, 111 (2012) 483-489.
- 638 [5] N. Akther, S. Daer, Q. Wei, I. Janajreh, S.W. Hasan, Synthesis of polybenzimidazole (PBI)
639 forward osmosis (FO) membrane and computational fluid dynamics (CFD) modeling of
640 concentration gradient across membrane surface, *Desalination*, 452 (2019) 17-28.
- 641 [6] N. Akther, A. Sodiq, A. Giwa, S. Daer, H.A. Arafat, S.W. Hasan, Recent advancements in
642 forward osmosis desalination: A review, *Chemical Engineering Journal*, 281 (2015) 502-522.
- 643 [7] A. Tiraferri, C.D. Vecitis, M. Elimelech, Covalent binding of single-walled carbon
644 nanotubes to polyamide membranes for antimicrobial surface properties, *ACS Applied
645 Materials & Interfaces*, 3 (2011) 2869-2877.
- 646 [8] A. Giwa, N. Akther, V. Dufour, S.W. Hasan, A critical review on recent polymeric and
647 nano-enhanced membranes for reverse osmosis, *RSC Advances*, 6 (2016) 8134-8163.
- 648 [9] S. Lim, V.H. Tran, N. Akther, S. Phuntsho, H.K. Shon, Defect-free outer-selective hollow
649 fiber thin-film composite membranes for forward osmosis applications, *Journal of Membrane
650 Science*, 586 (2019) 281-291.
- 651 [10] Q.V. Ly, Y. Hu, J. Li, J. Cho, J. Hur, Characteristics and influencing factors of organic
652 fouling in forward osmosis operation for wastewater applications: A comprehensive review,
653 *Environment International*, 129 (2019) 164-184.
- 654 [11] M. Liu, S. Yu, J. Tao, C. Gao, Preparation, structure characteristics and separation
655 properties of thin-film composite polyamide-urethane seawater reverse osmosis membrane,
656 *Journal of Membrane Science*, 325 (2008) 947-956.
- 657 [12] R. Reis, L.F. Dumée, B.L. Tardy, R. Dagastine, J.D. Orbell, J.A. Schutz, M.C. Duke,
658 Towards Enhanced Performance Thin-film Composite Membranes via Surface Plasma
659 Modification, *Scientific Reports*, 6 (2016) 29206.
- 660 [13] C.Y. Tang, Y.-N. Kwon, J.O. Leckie, Effect of membrane chemistry and coating layer on
661 physiochemical properties of thin film composite polyamide RO and NF membranes: II.
662 Membrane physiochemical properties and their dependence on polyamide and coating layers,
663 *Desalination*, 242 (2009) 168-182.
- 664 [14] Q.J. Niu, Reverse osmosis membrane with branched poly (alkylene oxide) modified
665 antifouling surface, in, *Google Patents*, 2007.
- 666 [15] G. Kang, M. Liu, B. Lin, Y. Cao, Q. Yuan, A novel method of surface modification on
667 thin-film composite reverse osmosis membrane by grafting poly(ethylene glycol), *Polymer*, 48
668 (2007) 1165-1170.
- 669 [16] N. Akther, S. Lim, V.H. Tran, S. Phuntsho, Y. Yang, T.-H. Bae, N. Ghaffour, H.K. Shon,
670 The effect of Schiff base network on the separation performance of thin film nanocomposite
671 forward osmosis membranes, *Separation and Purification Technology*, 217 (2019) 284-293.
- 672 [17] S. Lim, N. Akther, V.H. Tran, T.-H. Bae, S. Phuntsho, A. Merenda, L.F. Dumée, H.K.
673 Shon, Covalent organic framework incorporated outer-selective hollow fiber thin-film

674 nanocomposite membranes for osmotically driven desalination, *Desalination*, 485 (2020)
675 114461.

676 [18] G. Zhao, R. Hu, Y. He, H. Zhu, Physically Coating Nanofiltration Membranes with
677 Graphene Oxide Quantum Dots for Simultaneously Improved Water Permeability and Salt/Dye
678 Rejection, *Advanced Materials Interfaces*, 6 (2019) 1801742.

679 [19] X. Song, L. Wang, C.Y. Tang, Z. Wang, C. Gao, Fabrication of carbon nanotubes
680 incorporated double-skinned thin film nanocomposite membranes for enhanced separation
681 performance and antifouling capability in forward osmosis process, *Desalination*, 369 (2015)
682 1-9.

683 [20] M. Ghanbari, D. Emadzadeh, W.J. Lau, T. Matsuura, A.F. Ismail, Synthesis and
684 characterization of novel thin film nanocomposite reverse osmosis membranes with improved
685 organic fouling properties for water desalination, *RSC Advances*, 5 (2015) 21268-21276.

686 [21] N. Akther, Z. Yuan, Y. Chen, S. Lim, S. Phuntsho, N. Ghaffour, H. Matsuyama, H. Shon,
687 Influence of graphene oxide lateral size on the properties and performances of forward osmosis
688 membrane, *Desalination*, 484 (2020).

689 [22] S. Lim, K.H. Park, V.H. Tran, N. Akther, S. Phuntsho, J.Y. Choi, H.K. Shon, Size-
690 controlled graphene oxide for highly permeable and fouling-resistant outer-selective hollow
691 fiber thin-film composite membranes for forward osmosis, *Journal of Membrane Science*,
692 (2020) 118171.

693 [23] S.Y. Lee, H.J. Kim, R. Patel, S.J. Im, J.H. Kim, B.R. Min, Silver nanoparticles
694 immobilized on thin film composite polyamide membrane: characterization, nanofiltration,
695 antifouling properties, *Polymers for Advanced Technologies*, 18 (2007) 562-568.

696 [24] N. Akther, S. Phuntsho, Y. Chen, N. Ghaffour, H.K. Shon, Recent advances in
697 nanomaterial-modified polyamide thin-film composite membranes for forward osmosis
698 processes, *Journal of Membrane Science*, 584 (2019) 20-45.

699 [25] H.M. Hegab, A. ElMekawy, T.G. Barclay, A. Michelmores, L. Zou, C.P. Saint, M. Ginic-
700 Markovic, Fine-tuning the surface of forward osmosis membranes via grafting graphene oxide:
701 Performance patterns and biofouling propensity, *ACS Applied Materials & Interfaces*, 7 (2015)
702 18004-18016.

703 [26] H. Jin, F. Rivers, H. Yin, T. Lai, P. Cay-Durgun, A. Khosravi, M.L. Lind, P. Yu, Synthesis
704 of AgCl mineralized thin film composite polyamide membranes to enhance performance and
705 antifouling properties in forward osmosis, *Industrial & Engineering Chemistry Research*, 56
706 (2017) 1064-1073.

707 [27] J. Nikkola, J. Sievänen, M. Raulio, J. Wei, J. Vuorinen, C.Y. Tang, Surface modification
708 of thin film composite polyamide membrane using atomic layer deposition method, *Journal of*
709 *Membrane Science*, 450 (2014) 174-180.

710 [28] A. Soroush, W. Ma, M. Cyr, M.S. Rahaman, B. Asadishad, N. Tufenkji, In situ silver
711 decoration on graphene oxide-treated thin film composite forward osmosis membranes:
712 Biocidal properties and regeneration potential, *Environmental Science & Technology Letters*,
713 3 (2016) 13-18.

714 [29] T. Jin, Y. Ma, W. Matsuda, Y. Masuda, M. Nakajima, K. Ninomiya, T. Hiraoka, J.-y.
715 Fukunaga, Y. Daiko, T. Yazawa, Preparation of surface-modified mesoporous silica
716 membranes and separation mechanism of their pervaporation properties, *Desalination*, 280
717 (2011) 139-145.

718 [30] V. Vatanpour, M. Kaviani, Synergistic effect of silica nanoparticles in the matrix of a
719 poly(ethylene glycol) diacrylate coating layer for the surface modification of polyamide
720 nanofiltration membranes, *Journal of Applied Polymer Science*, 133 (2016).

721 [31] Z. Wang, X. Jiang, X. Cheng, C.H. Lau, L. Shao, Mussel-inspired hybrid coatings that
722 transform membrane hydrophobicity into high hydrophilicity and underwater

723 superoleophobicity for oil-in-water emulsion separation, *ACS Applied Materials & Interfaces*,
724 7 (2015) 9534-9545.

725 [32] L. Xing, N. Guo, Y. Zhang, H. Zhang, J. Liu, A negatively charged loose nanofiltration
726 membrane by blending with poly (sodium 4-styrene sulfonate) grafted SiO₂ via SI-ATRP for
727 dye purification, *Separation and Purification Technology*, 146 (2015) 50-59.

728 [33] L. Zhang, Y. Lin, H. Wu, L. Cheng, Y. Sun, T. Yasui, Z. Yang, S. Wang, T. Yoshioka, H.
729 Matsuyama, An ultrathin in situ silicification layer developed by an electrostatic attraction
730 force strategy for ultrahigh-performance oil–water emulsion separation, *Journal of Materials*
731 *Chemistry A*, 7 (2019) 24569-24582.

732 [34] S. Daer, N. Akther, Q. Wei, H.K. Shon, S.W. Hasan, Influence of silica nanoparticles on
733 the desalination performance of forward osmosis polybenzimidazole membranes, *Desalination*,
734 491 (2020) 114441.

735 [35] K. Huang, X. Quan, X. Li, F.H. Tezel, B. Li, Improved surface hydrophilicity and
736 antifouling property of nanofiltration membrane by grafting NH₂-functionalized silica
737 nanoparticles, *Polymers for Advanced Technologies*, 29 (2018) 3159-3170.

738 [36] N. Akther, S.M. Ali, S. Phuntsho, H. Shon, Surface modification of thin-film composite
739 forward osmosis membranes with polyvinyl alcohol–graphene oxide composite hydrogels for
740 antifouling properties, *Desalination*, 491 (2020) 114591.

741 [37] S. Romero-Vargas Castrillón, X. Lu, D.L. Shaffer, M. Elimelech, Amine enrichment and
742 poly(ethylene glycol) (PEG) surface modification of thin-film composite forward osmosis
743 membranes for organic fouling control, *Journal of Membrane Science*, 450 (2014) 331-339.

744 [38] B. Scheibe, E. Borowiak-Palen, R. Kalenczuk, Effect of the silanization processes on the
745 properties of oxidized multiwalled carbon nanotubes, *Acta Physica Polonica, A.*, 116 (2009).

746 [39] C.C.M.C. Carcouët, M.W.P. van de Put, B. Mezari, P.C.M.M. Magusin, J. Laven, P.H.H.
747 Bomans, H. Friedrich, A.C.C. Esteves, N.A.J.M. Sommerdijk, R.A.T.M. van Benthem, G. de
748 With, Nucleation and growth of monodisperse silica nanoparticles, *Nano Letters*, 14 (2014)
749 1433-1438.

750 [40] D.J. Belton, O. Deschaume, C.C. Perry, An overview of the fundamentals of the chemistry
751 of silica with relevance to biosilicification and technological advances, *FEBS Journal*, 279
752 (2012) 1710-1720.

753 [41] G.S. Lai, W.J. Lau, P.S. Goh, A.F. Ismail, Y.H. Tan, C.Y. Chong, R. Krause-Rehberg, S.
754 Awad, Tailor-made thin film nanocomposite membrane incorporated with graphene oxide
755 using novel interfacial polymerization technique for enhanced water separation, *Chemical*
756 *Engineering Journal*, 344 (2018) 524-534.

757 [42] C.Y. Tang, Y.-N. Kwon, J.O. Leckie, Effect of membrane chemistry and coating layer on
758 physiochemical properties of thin film composite polyamide RO and NF membranes: I. FTIR
759 and XPS characterization of polyamide and coating layer chemistry, *Desalination*, 242 (2009)
760 149-167.

761 [43] G. De, B. Karmakar, D. Ganguli, Hydrolysis–condensation reactions of TEOS in the
762 presence of acetic acid leading to the generation of glass-like silica microspheres in solution at
763 room temperature, *Journal of Materials Chemistry*, 10 (2000) 2289-2293.

764 [44] K.-M. Li, J.-G. Jiang, S.-C. Tian, X.-J. Chen, F. Yan, Influence of silica types on synthesis
765 and performance of amine–silica hybrid materials used for CO₂ capture, *The Journal of*
766 *Physical Chemistry C*, 118 (2014) 2454-2462.

767 [45] S. Sánchez, M. Pumera, E. Fàbregas, J. Bartrolí, M.J. Esplandiú, Carbon
768 nanotube/polysulfone soft composites: Preparation, characterization and application for
769 electrochemical sensing of biomarkers, *Physical Chemistry Chemical Physics*, 11 (2009) 7721-
770 7728.

- 771 [46] B. Hu, L. Liu, Y. Zhao, C. Lü, A facile construction of quaternized polymer brush-grafted
772 graphene modified polysulfone based composite anion exchange membranes with enhanced
773 performance, *RSC Advances*, 6 (2016) 51057-51067.
- 774 [47] H. Hafeez, D.K. Choi, C.M. Lee, P.J. Jesuraj, D.H. Kim, A. Song, K.B. Chung, M. Song,
775 J.F. Ma, C.-S. Kim, S.Y. Ryu, Replacement of n-type layers with a non-toxic APTES interfacial
776 layer to improve the performance of amorphous Si thin-film solar cells, *RSC Advances*, 9
777 (2019) 7536-7542.
- 778 [48] W.J. Lau, A.F. Ismail, P.S. Goh, N. Hilal, B.S. Ooi, Characterization methods of thin film
779 composite nanofiltration membranes, *Separation & Purification Reviews*, 44 (2015) 135-156.
- 780 [49] H.-C. Yang, J.-K. Pi, K.-J. Liao, H. Huang, Q.-Y. Wu, X.-J. Huang, Z.-K. Xu, Silica-
781 decorated polypropylene microfiltration membranes with a mussel-inspired intermediate layer
782 for oil-in-water emulsion separation, *ACS Applied Materials & Interfaces*, 6 (2014) 12566-
783 12572.
- 784 [50] M. Liu, Q. Chen, L. Wang, S. Yu, C. Gao, Improving fouling resistance and chlorine
785 stability of aromatic polyamide thin-film composite RO membrane by surface grafting of
786 polyvinyl alcohol (PVA), *Desalination*, 367 (2015) 11-20.
- 787 [51] L.M. Jin, S.L. Yu, W.X. Shi, X.S. Yi, N. Sun, Y.L. Ge, C. Ma, Synthesis of a novel
788 composite nanofiltration membrane incorporated SiO₂ nanoparticles for oily wastewater
789 desalination, *Polymer*, 53 (2012) 5295-5303.
- 790 [52] B. Mi, M. Elimelech, Chemical and physical aspects of organic fouling of forward osmosis
791 membranes, *Journal of Membrane Science*, 320 (2008) 292-302.
- 792 [53] Y. Mo, A. Tiraferri, N.Y. Yip, A. Adout, X. Huang, M. Elimelech, Improved antifouling
793 properties of polyamide nanofiltration membranes by reducing the density of surface carboxyl
794 groups, *Environmental Science & Technology*, 46 (2012) 13253-13261.
- 795 [54] M. Rastgar, A. Shakeri, A. Bozorg, H. Salehi, V. Saadattalab, Highly-efficient forward
796 osmosis membrane tailored by magnetically responsive graphene oxide/Fe₃O₄ nanohybrid,
797 *Applied Surface Science*, 441 (2018) 923-935.

798